RESEARCH METHODS

The Duke Mouse Brain Atlas: MRI and light sheet microscopy stereotaxic atlas of the mouse brain

Harrison Mansour[1], Ryan Azrak[1], James J. Cook[1], Kathryn J. Hornburg[1], Yi Qi[1], Yuqi Tian[1], Robert W. Williams[2], Fang-Cheng Yeh[3], Leonard E. White[1,4], G. Allan Johnson[1]*

Atlases of the brain are critical resources that make it possible to share data in a common reference frame. Unexpectedly, there is no three-dimensional (3D) stereotaxic atlas of the mouse brain that provides whole brain coverage at macro to single-cell levels. Diffusion tensor images from five perfusion-fixed (in skull) specimens were acquired at 15 micrometers, the highest resolution ever reported. Diffusion tensor imaging yields multiple 3D volumes, each of which highlights unique cytoarchitecture. The averages were mapped into micro–computed tomography of the mouse skull to create external landmarks (bregma and lambda). Light sheet images of the same brains were coregistered, providing cell maps in the same stereotaxic space. The Allen Reference Atlas was registered to the volume to correct the geometric distortion in that atlas and bring it into the stereotaxic space. The resulting multiscalar (13 terabytes) atlas provides a common spatial framework to anneal data across molecular, structural, and functional studies of mice.

INTRODUCTION

Similarities in structure and function across mammalian species, ease of genetic manipulation, and the wide range of models of neurologic diseases have made the mouse one of the most widely used models for neurologic research. Consequently, a diverse range of atlases has evolved to coordinate research across multiple laboratories using multiple methodologies at multiple scales. The stereotaxic atlas of Franklin and Paxinos (FP), based on conventional Nissl and acetylcholinesterase sections, has been a critical resource for anatomical reference because of its standardized labeling and ontology (*1*, *2*). However, the sampling is not contiguous or uniform along all three axes. The Allen Mouse Brain Atlas (ABA) introduced in 2008 was constructed from serial Nissl sections (*3*). The Common Coordinate Framework (CCFv3) published in 2020 was constructed from serial two photon sections using autofluorescence (*4*). Both suffer distortions from tissue processing outside the skull. Waxholm space (WHS) introduced a three-dimensional (3D) isotropic atlas based on magnetic resonance imaging (MRI) in the skull, but the spatial and contrast resolution were limited and stereotaxic landmarks were not included (*5*). Table S1 summarizes some of the many atlases that have been created thus far. Whole brain stereotaxic atlases based on 2D sections are commonly available. However, there has been no whole brain 3D stereotaxic atlas at microscopic resolution.

We have addressed this need using magnetic resonance histology (MRH), i.e., MRI of postmortem specimens at microscopic resolution (*6*) and light sheet microscopy (LSM) of five C57BL/6J mouse brains in a stereotaxic space defined by micro–computed tomography (micro-CT) (Fig. 1). The resulting Duke Mouse Brain Atlas (DMBA) has the highest spatial and contrast resolution with the most comprehensive catalog of imaging contrasts yet reported. The result is a whole brain, stereotaxic atlas enabling data sharing across voxel volumes ranging over five orders of magnitude. Researchers generating in vivo functional MRI and structural MRI at 10^{-3} mm^3, cytoarchitecture at 10^{-6} mm^3, connectomics at 10^{-7} mm^3, and individual cells at 10^{-8} mm^3 will all be able to map their data into the common stereotaxic space defined by the DMBA. Diffusion tensor images and gradient echo images provide unprecedented contrast in 14 complementary 3D volumes, each highlighting distinct cytoarchitecture, e.g., cortical layers, nuclear boundaries, and white matter tracts. Super-resolution track density images (TDIs) enable connectome analysis at 25,000X the spatial resolution of in vivo studies. The same tissues scanned with LSM, corrected for geometric distortion and mapped into the stereotaxic space, provide 17 different molecular cell stains. The CCFv3 labels complete the multimodal atlas (*4*, *7*).

The utility of this multimodal atlas is demonstrated by registering the autofluorescent images of the CCFv3 into the corrected stereotaxic space defined in the DMBA, bringing the extraordinary collection in the CCFv3 into stereotaxic coordination. The breadth of contrast in the DMBA can be used to routinely map light sheet volumes that suffer geometric distortion from tissue swelling or shrinkage into stereotaxic registration. This corrects regional volumes measured in the uncorrected LSM images, which can differ from in vivo measures by as much as 80%.

RESULTS

Overview

The unifying core of the atlas is a library of 3D MRH volumes derived from five 90- ± 2-day C57BL/6J male mice (table S2). Multigradient echo (mGRE) and diffusion-weighted MRI (dMRI) were acquired at 15-μm isotropic spatial resolution with the brains in the skull limiting global or regional swelling or shrinkage and preventing any further volumetric distortion or tissue destruction that might otherwise accompany cranial dissection and conventional histology. The MRH volumes for all five specimens were diffeomorphically registered together, increasing the contrast to noise. Fourteen different average volumes were derived from the collection of MRH scans, each highlighting different meso- and microscopic features of cerebral tissue (table S3). Micro-CT images (@ 25-μm isotropic resolution) were

[1]Duke Center for In Vivo Microscopy, Departments of Radiology and Biomedical Engineering, Duke University, Durham, NC, USA. [2]Department of Genetics, Genomics and Informatics, University of Tennessee Health Science Center, Memphis, TN, USA. [3]Department of Neurological Surgery, University of Pittsburgh, Pittsburgh, PA, USA. [4]Department of Neurology, Duke University, Durham, NC, USA.
*Corresponding author. Email: gjohnson@duke.edu

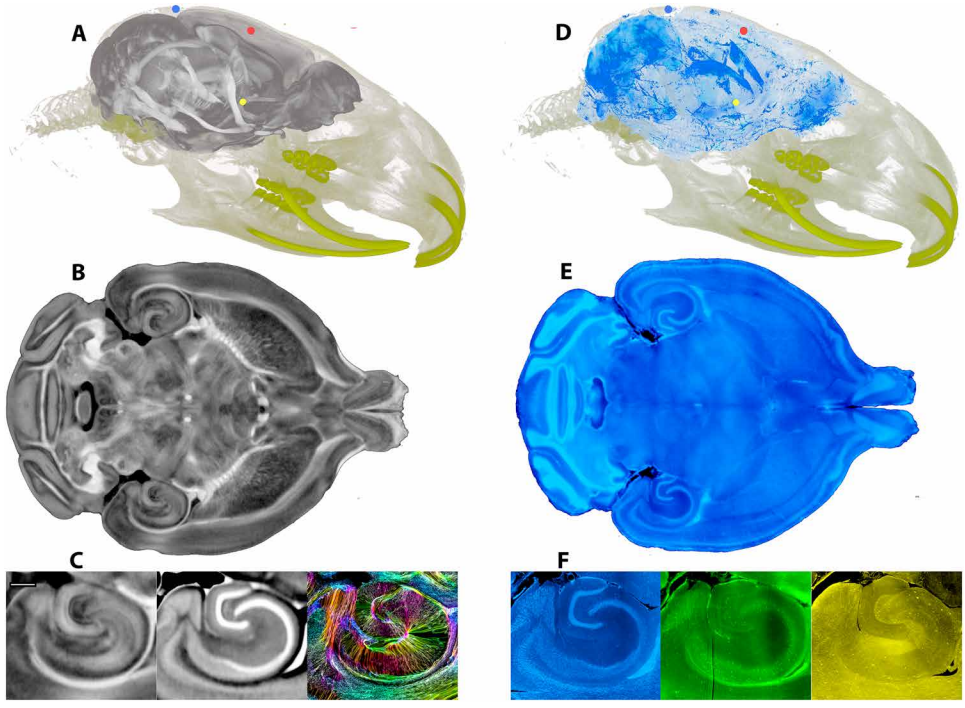

Fig. 1. The DMBA combines 3D MRH and LSM of the C57BL/6J mouse brain in a stereotaxic space. That space [(A) to (C)] is defined by MRH of five males with brains in the skull minimizing distortion. mGRE and DTI sequences highlight different features of cerebral tissue. Specimens were registered to an MDT to create average 3D volumes. (**A**) Micro-CT image of the skull was registered to the MRH providing landmarks (lambda: blue; bregma: red; AC: yellow). (**B**) Axial slice from the FA volume demonstrates myeloarchitecture. (**C**) Comparisons of the hippocampus in three MRH modalities. Left: FA; middle: MD; right: TDIs. Additional volumes provide more detail (fig. S1 and table S3). (**D**) LSM images were generated in the same brains and registered to the MRH volumes. The image shows corrected whole brain NeuN. (**E**) Representative axial slice at full resolution. (**F**) Inspection of this image and two additional stains shows the same hippocampal region as in (C) with spatial resolution sufficient to resolve single cells. Left: individual cells positive for NeuN; middle: cells positive for parvalbumin; right: cells positive for neuropeptide Y. Scale bar in (C), 0.4 mm.

registered to the MRH average volume to provide critical cranial landmarks (bregma and lambda). The brains used for the MRH volumes were then removed from the skull, cleared, labeled with 15 different immunohistochemical markers, and processed for LSM. A specimen in which cells expressing the Thy-1 cell surface antigen were visualized with genetically encoded yellow fluorescent protein (YFP) (*8*) was also scanned with the MRH protocol but was not included in the MRH atlas. An LSM volume from this specimen is included. The specimens summarized in table S4 were scanned using selective plane illumination microscopy at cellular resolution (1.8 by 1.8 by 4.0 μm). These LSM images were registered at full resolution to the DMBA, correcting the geometric distortion common in LSM and placing them in the stereotaxic space (*9*). The registered dMRI volumes in the common space were used to create super-resolution (5 μm) TDIs (*10*). A subset of isotropic 3D labels from the common coordinate reference framework (CCFv3) (*4*) was registered to the average MRH volumes, placing these widely used labels in the stereotaxic space.

Average MRH atlas

In a previous work, we have described dMRI and mGRE images acquired at 15-μm isotropic resolution (*7*). This stereotaxic atlas expands on that in four critical ways by creating average dMRI and mGRE volumes with much higher contrast to noise, mapping everything into the stereotaxic space with cranial landmarks from micro-CT, generation of an average light sheet atlas (NeuN) in the same stereotaxic space, and the addition of 17 LSM volumes (in the stereotaxic space) with unique immunohistochemistry stains. Figure 2 demonstrates how the contrast resolution has improved in the MRH.

The improvement in contrast to noise is similar across all the average images, resulting in one of the most unique features of this atlas, the definition of mesoscale structures seen in Fig. 3. Hippocampal and cerebellar layers not seen in the gradient recalled image (Fig. 3A) become readily visible in the diffusion-weighted image (DWI) (Fig. 3B). The Purkinje cell layer in the cerebellar cortex is visible in the mean diffusivity (MD) image (Fig. 3D) and subtle features of cerebellar white matter in the lobules are revealed in the fractional anisotropy (FA) image (Fig. 3G). The color FA image in Fig. 3H provides evidence of specific orientation of these fascicles. Table S3 summarizes the 14 volumes included in the MRH atlas. Most of the volumes are provided with the skull stripped as this facilitates their use in automated registration to other atlases. An average mGRE without masking is provided to help mapping in vivo MRI data. Figure S1 shows a full field representative axial plane at full resolution, allowing the reader to examine a larger region of interest (ROI) interactively.

Averaging five specimens produces a few confounds. High contrast penetrating vessels in similar but not identical areas will "shine through" in the average atlas, giving one an impression of higher vascular density, as shown in fig. S2. Figure S3 demonstrates the blurring one might expect by focusing on modular features of brain cytoarchitecture, such as the glomeruli in the olfactory bulb. They are discrete and well defined in the images from the individual specimens

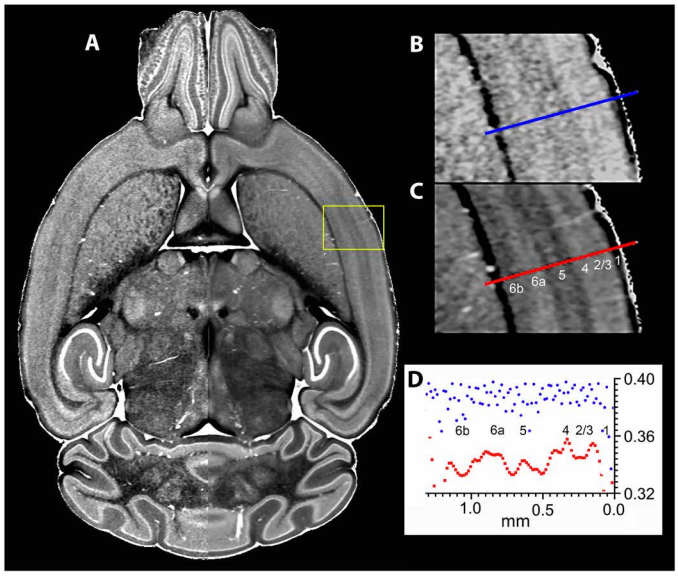

Fig. 2. Precision registration improves image contrast and signal to noise. (**A**) A single animal (left side, case200302-1:1, MD contrast) compared to the average of five cases (right side; QSDR). (**B**) Neocortex (primary somatic sensory cortex) highlighted in (A) for the single specimen and (**C**) for the same region from the MD average image, with traces defining a plot across both and numerical labels to indicate cortical layers. (**D**) The gray scale value across the single specimen (blue) is noisy, with cortical layers poorly differentiated. The plot across the same area in the MD average (red) clearly defines cytoarchitectonic borders between cortical layers and even sublamination in cortical layer 5. Similarly, other cytoarchitectural features of the thalamic nuclei and cerebellar cortex, including the Purkinje cell layer, are more distinct in the average image. Nonlinear gray scale enhancement was applied in Photoshop to both halves of the figure to enable appreciation of changes in contrast to noise.

before averaging. After averaging, they are blurred, but the layers of the olfactory bulb defined by intrinsic cytoarchitectural features are enhanced.

Stereotaxic CT

Five 3D micro-CT images were acquired at 25-μm isotropic spatial resolution to provide cranial landmarks (bregma and lambda) for defining the stereotaxic space. Each CT volume was aligned to the average MRH volume using an affine transform to estimate the potential biological variability one might encounter in a real-world stereotaxic environment (see Materials and Methods). The largest outlier was a displacement of 450 μm between a single volume and the average of the five. The DMBA includes two collections of data (MRH and LSM) in the common space (Fig. 1): A volume rendered view of the CT data combined with the DWI (fig. S4A) includes the incisors used in stereotaxic frames to establish the coronal plane. Figure S4B provides a midsagittal slice of the combined CT and DWI focused on the DWI with bregma marked with a red dot and lambda with a blue dot. A third landmark in the center of the anterior commissure (AC; yellow dot) defines the coronal plane as the plane intersecting bregma and the AC. The coronal plane for lambda is shown in fig. S4C, and the coronal plane for bregma is shown in fig. S4D. We have chosen this orientation to be consistent with that used by FP (*2*, *11*). Figure S5 shows the midsagittal plane for the DMBA-DWI and the sagittal Nissl image from ref. (*11*) (Plate 104). The estimate of the "flat skull" angle has been marked for both along with the angle of the corpus callosum, which differs by less than 0.5° between atlases. The FP atlas has been used by many to guide stereotaxic surgery. Figure S6 was created by aligning the grids of the FP atlas to the grids in the DMBA. These grids are anchored in bregma and the AC. Superimposing the FP labels on the coronal MD image from the DMBA at bregma and the FP midsagittal with the midsagittal MD image from the DMBA allows one to appreciate potential differences in stereotaxic placement. Agreement is within 300 μm across most of the volume, well within the variation one might expect across animals.

Labels

We have adopted a version of the CCFv3 (*4*) as the default labels and ontology for the atlas. CCFv3 delineates a total of 461 structures. The DMBA label set includes a subset of 308 (154 in each hemisphere: 137 gray matter, 17 white matter, and 4 ventricular) structures. The entire CCFv3 label set was mapped to the DMBA by first registering the CCFv3 autofluorescent image to a composite image created from the b_0 and DWI of the DMBA using a registration pipeline optimized for the mouse brain (*7*, *12*). The pipeline, which is built on the Advanced Normalization Tool kit (*13*), started with an initial linear transform followed by affine and diffeomorphic transforms. The aggregate transform was applied to the full CCFv3 label set to bring it into registration with the DMBA. Data were then manually inspected and corrected by displaying three orthogonal planes using at least two different volumes from the scalar diffusion tensor images as demonstrated in Fig. 4. Slicer (https://slicer.org/) allowed simultaneous display of three cardinal axes using at least two different sources of contrast. In several instances, the MD or color generalized q sampling imaging (GQI) image informed the decisions on adjusting boundaries. Figure S7 shows a magnified coronal section in the thalamus with the CCFv3 autofluorescent image and the five different scalar dMRI images in the DMBA that were used to assist boundary definition. The atlas is used routinely for labeling MRH volumes of many strains other than the C57BL/6J and translating labels between MRH and LSM volumes with widely different histochemical stains (*9*). Smaller, poorly registered ROIs), such as neocortical laminae or subdivisions of subcortical nuclei, pose a technical source of noise that can affect the validity of the registration (*7*, *14*). We describe an intermediate path with the reduced CCFv3 (RCCFv3) label set in which related structures with volumes < 0.1 mm^3 have been aggregated into larger volumes of which the structures are subcomponents. The full list of structures (DMBA_Labels), abbreviations, and relations between CCFv3 and RCCFv3 can be downloaded with the atlas from the FAIR website (https://civmimagespace.civm.duhs.duke.edu/). The RCCFv3 labels were iteratively adjusted by two experienced neuroanatomists (L.E.W. and R.W.W.) using simultaneous display of at least two unique sources of contrast in all three planes. The creation of this atlas has made clear that improved labeling will be possible in the future with the combination of light sheet with better MR images. That process is underway. The accompanying JSON file (RCCFv3_JSON) provides explicit description for all the columns. Table S5 lists the RCCFv3 and Allen Reference Atlas labels and abbreviations.

Diffusion tensor data

The scalar images of anatomy described above are derived using the diffusion tensor imaging (DTI) algorithm and analogous GQI algorithm

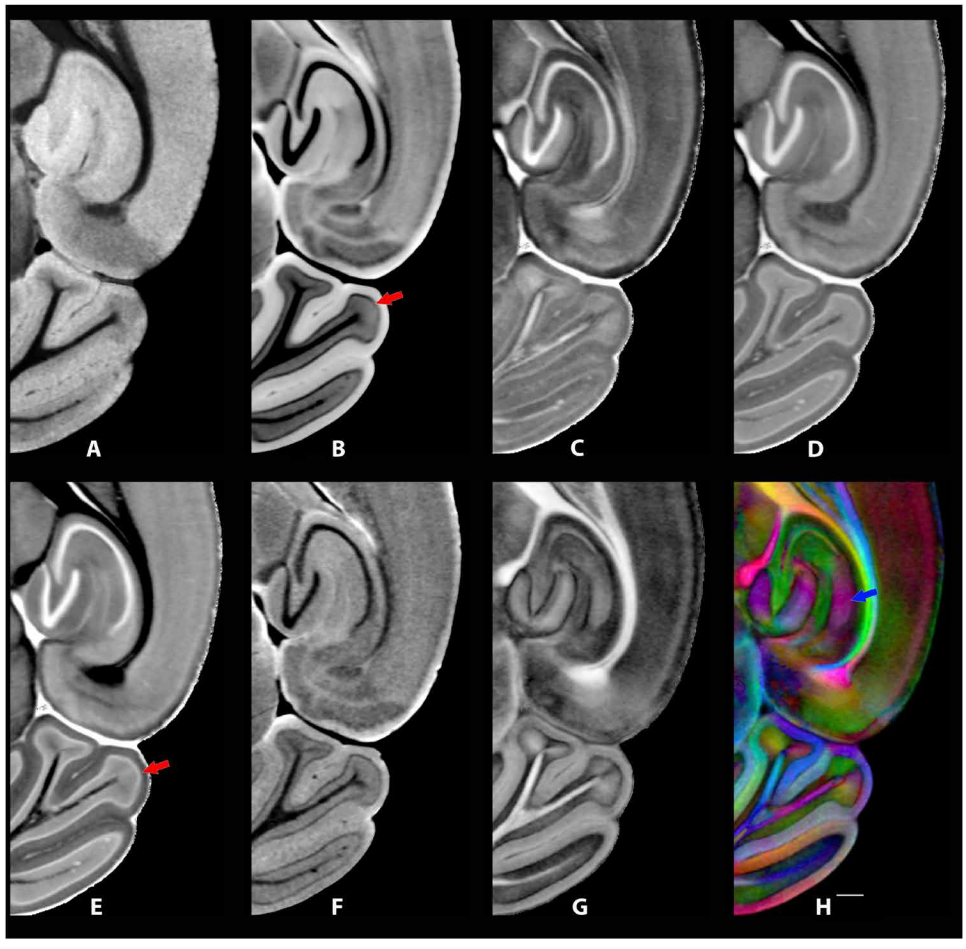

Fig. 3. Magnified sections from eight of the volumes from the average MRH atlas show the marked improvements in definition of cytoarchitectural boundaries. (**A**) Average of four echoes from the mGRE. (**B**) DWI. (**C**) Axial diffusivity. (**D**) MD. (**E**) Radial diffusivity. (**F**) ISO from the GQI algorithm. (**G**) FA from the DTI algorithm. (**H**) Color FA (ClrFA) from the DTI algorithm. Each MRH contrast reveals anatomic features differentially; together, they provide enriched opportunity to recognize cytoarchitectural boundaries. For example, the Purkinje cell layer of the cerebellar cortex is revealed by bright signal in the radial diffusivity volume [red arrow in (E)] and dark signal in the diffusion-weighted volume [red arrow in (B)]. In the hippocampus, the radial organization of apical dendrites of CA1 arrow in (H). Scale bar in (H), 0.4 mm. Nonlinear gray scale enhancement was applied in Photoshop to accommodate the high dynamic range of some of the images [(B), (D), (E), (G)].

(*15*, *16*) (see table S3). These algorithms provide the basis for defining whole brain connectivity (*17*–*20*). The challenge in tractography lies in resolving crossing and merging fibers. We have used the GQI algorithm because it addresses this challenge through the use of high angular resolution diffusion imaging (*21*). There is a robust literature addressing trade-offs in spatial and angular resolution (*22*–*24*) and the efficacy (*25*). Because the data are 3D, comparing resolution across protocols should use voxel volume. The connectome data in this atlas address the enormous differences between clinical scans acquired at 2-mm resolution (8 mm^3 voxels) and 15-μm^3 voxels that are 2.4×10^6 times smaller. Because the voxels are so much smaller, there will be far fewer crossing fibers in each voxel, which, in turn, will lead to a reduction in tracking errors in each voxel. However, because there are more voxels, it is not clear that there will be an aggregate reduction in false tracks. The number of angular samples one acquires also helps resolve crossing fibers. The resolution index is the product of the angular and spatial resolution (no. of angles sampled per voxel volume) (*26*) . For reference, the resolution index in the human connectome is 527 angular samples/mm^3 (*23*). In our previous work, we found good agreement between DTI and the results of conventional in vivo tract-tracing experiments using retroviral tracers in a mouse with DTI datasets at a resolution index of 1.51×10^6 angles/mm^3 (*20*). The resolution index for the DMBA at 3.2×10^7 samples/mm^3 is more than 20 times that of our previous work, making this the highest resolution connectome of the mouse brain available to date. Figure S8 shows the connectome of one of the individual specimens and that of five specimens that have been averaged together using the q space diffeomorphic resconstruction (QSDR) method (*16*). Improvement in the sensitivity is clear, especially for connections within and across the cerebral hemispheres (intracortical and subcortical fiber tracts, including commissural tracts). Such connectome data are representative of ongoing work to validate the node-/edge-specific results in quantitative terms and in relationship to experiments with axonal tracers—a necessary step toward creation of a white matter atlas of the mouse brain.

Population NeuN

Contrast defining cytoarchitectural boundaries and myeloarchitectural structures, in MRH and LSM images, is dependent on completely different phenomena (e.g., diffusion of water versus immunohistochemical receptor sites). This presents a challenge to algorithms matching similarity or strong mutual information. We have optimized

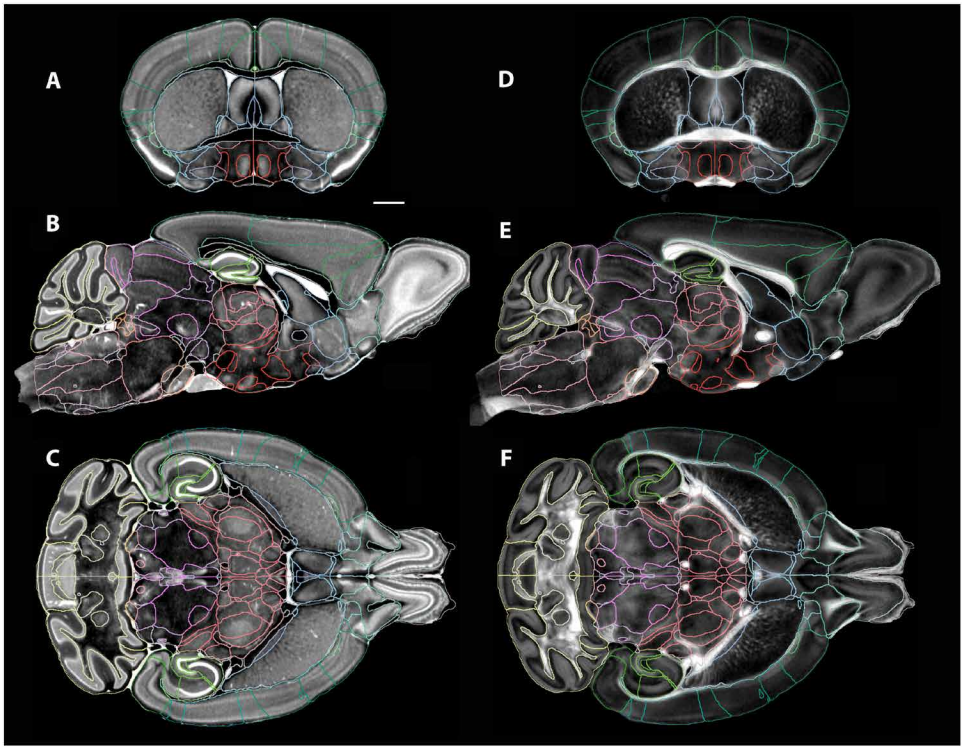

Fig. 4. Multiple dMRI volumes provide complimentary contrast to support labels. Previously (*14*), we found that our workflow could reliably register ROIs with volumes greater than 0.1 mm^3 across four strains (C57BL/6J, DBA/2J, CAST/EiJ, and BTBR T^+Itpr3^{tf}/J) with coefficients of variation between the left and right hemisphere of less than 5%. The relations between structures and related subvolumes in RCCFv3 and the similar structures in CCFv3 are included in the Excel data sheet available with the download of the atlas. The RCCFv3 labels are shown on the MD volume (**A** to **C**) and the FA volume (**D** to **F**). The labels are isotropic and color coded to correspond with the standard used in the ABA (https://atlas.brain-map.org/atlas). Scale bar, 1 mm.

the registration between MRH and LSM based on DWI and MD and NeuN (*9*). Figure S9A shows a comparison of the DMBA MD image with a minimum deformation template (MDT) created from four LSM NeuN images (table S4, Specimens 220905_1 to 4). Although there is no precise correspondence between the signals in the two images, there are several regions well distributed throughout the volume with consistent signal relations that help drive the registration. These are formalin-fixed tissues that have been heavily doped with a contrast agent, so sorting out signal dependences is complex. However, there are some consistent observations. For example, cell-dense regions yield high signal in MD. The intracellular diffusion coefficient in cells is low so the signal is high in a DWI. A high density of cells in which diffusion signal decay is minimal is a plausible interpretation. As a marker of neuronal nuclei, one should expect that brain structures with high neuronal density should correspond to those high-signal regions in MD images. This is evident across the brain with notable examples in the granule and pyramidal cell layers of the hippocampus, the granule cell layer of the cerebellar cortex, the granule cell layer of the olfactory bulb, and the granular and supragranular layers of the neocortex. Figure S9 (B and C) highlights the alignment of the 15-μm MDT NeuN (B) with an individual volume (220905-1_2) at full resolution (1.8 by 1.8 μm), where individual neurons are clearly seen (C).

Grids

Six different grids are included with the atlas (see Materials and Methods), all indexed to bregma. These digitally generated grids are registered to the MRH volumes, which were acquired with the brain in the skull. As such, they represent the best estimate of the undistorted space. As noted below, they also provide a means to register the DMBA to the FP atlas. Three grids in *xy*, *xz*, and *xy* planes are defined at 1-mm spacing. The *xy* grid is visible in Fig. 5 and fig. S9A with the coronal and sagittal planes passing through bregma highlighted in thicker lines; other gridlines are equally spaced at 1-mm intervals off these planes. A second collection of three grids with 200-μm spacing is included, again indexed to bregma (see fig. S9, B and C).

FAIR distribution

DMBAvs2025.3.4 reported here is available at CIVMImageSpace (https://civmimagespace.civm.duhs.duke.edu/; 2024 Duke University. All Rights Reserved). The data were produced at the Duke School of Medicine, Department of Radiology and Pratt School of Engineering, Department of Biomedical Engineering and are being made available under a Creative Commons CC BY-NC-SA 4.0 License. See this URL for additional information (CC BY-NC-SA 4.0 Deed | Attribution-NonCommercial-ShareAlike 4.0 International | Creative Commons).

CIVMImageSpace has been constructed to handle very large multilayered (4D) image arrays and provide users the option of review to determine which data they would like to download. The site supports users who want full resolution and those who will benefit from lower resolution, more compact data. The aggregate library is ~13 TB. All data are displayed in RAS orientation. The data are grouped with FAIR standards and FAIR compliant metadata and

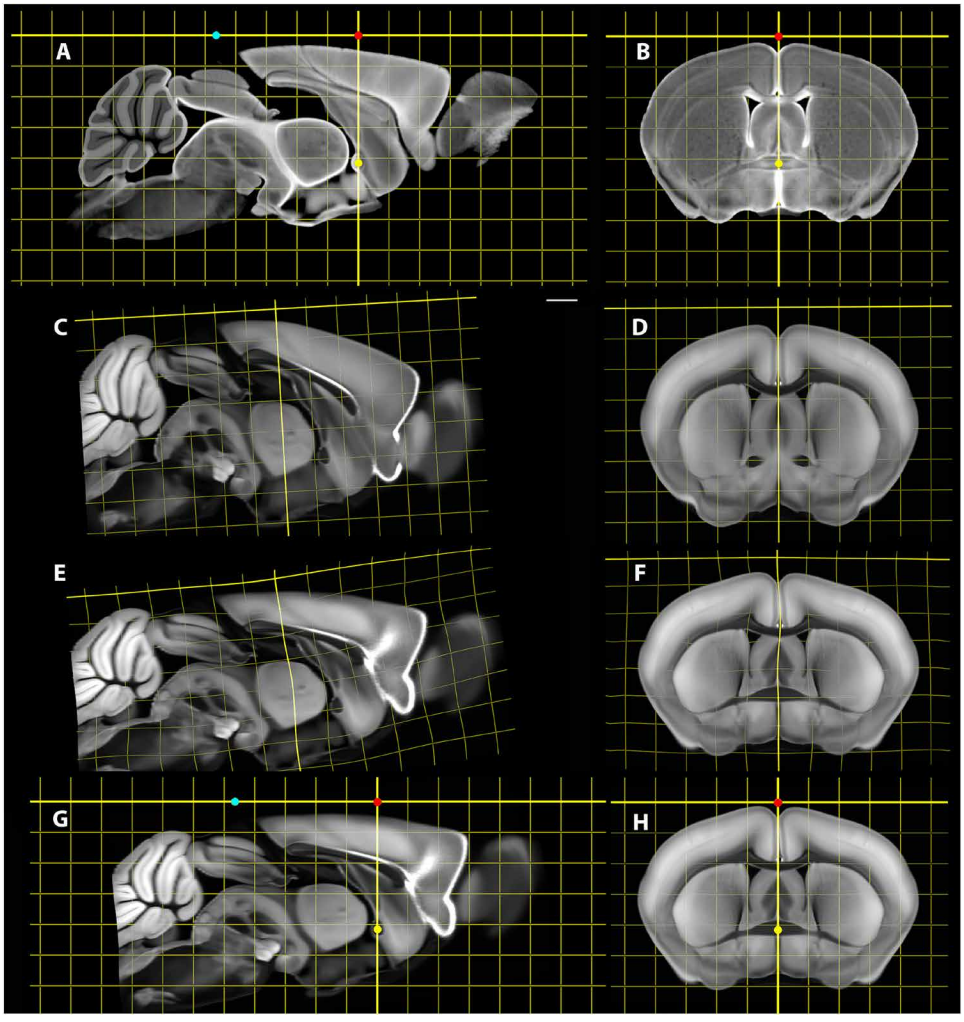

Fig. 5. Mapping the CCFv3 into the DMBA corrects distortion and places the CCFv3 in a stereotaxic space. A 3D grid was imposed into DMBA-DWI in (**A**) and (**B**). Because bregma and lambda are not defined in the CCFv3, we estimated their locations in CCFv3. CCFv3 was mapped into the DMBA. The transforms were inverted to map bregma into the CCFv3 space. A grid was defined in CCFv3 with an origin at bregma. (**C** and **D**) CCFv3 and grid, after affine warping to the DMBA, demonstrating global shrinkage in CCFv3 and alignment error of the *z* axis. This estimate returns a coronal slice at bregma, which misses the AC (D). (**E** and **F**) The geometric corrections are not uniform. CCFv3 is assembled from multiple brains, so this may be due to shrinkage or reconstruction. The *z* axis is tilted by ~4°. This occurs when the brain is removed from the cranial vault (*9*). The volume is stretched along *z* by ~4%. (D) and (F) highlight differential swelling. The swelling is 16.3% along the *y* axis and 5.7% along the *x* axis. (**G** and **H**) CCFv3 in the same stereotaxic frame as the DMBA, with corrected geometry and bregma and lambda. The results are consistent with a similar work of Perens *et al.* (*30*). Scale bar, 1 mm.

data files. Images are available to download as NRD files. N5 files are displayed on the website using a hierarchical display that allows users a more seamless interaction when there are bandwidth limitations. A web-enabled viewer (Neuroglancer) supports interactive review prior to download. This facilitates exploration without waiting for large volumes to download. The user chooses desired data and launches automated large queues. Consistent image headers across all volumes for RAS orientation facilitate interoperability of the volumes across multiple software packages.

Applications

The DMBA has been envisioned as a resource to bridge the gap across many neuroscience communities, including (i) preclinical imaging (MRI) studying mouse models of human disease, (ii) neuroscientists requiring precise and accurate coordinates for stereotaxic localization in experimental protocols, (iii) investigators needing to correct geometric distortion in light sheet and confocal microscopy, and (iv) those using multiple 3D volumes and needing to integrate data from diverse sources into a common reference space. We demonstrate the utility of the DMBA in two such examples.

The Common Coordinate Reference (CCFv3)

The CCFv3 (*4*) has become a unifying reference and resource across many domains of neuroscience. One major limitation in the CCFv3 is forthrightly stated: " ... at present, CCFv3 is not suitable for determining stereotaxic coordinates." (*4*). We demonstrate in Fig. 5 the use of the DMBA in making multiple improvements to the CCFv3. The DMBA corrects geometric distortion in the CCFv3 while providing cranial stereotaxic landmarks and additional sources of contrast to isolate mesoscale brain structures. The DMBA makes the

internal structure of mouse brain more accessible to preclinical MRI users, and it makes the multidimensional properties of MRH accessible to neuroscientists who are not yet familiar with MRI-based applications in mouse neuroscience.

Table S4 in Wang *et al.* (*4*) provides a summary of the average volumes of the structures in the CCFv3. The authors note that the atlas is not stereotaxic, so the absolute volumes are not accurate. The transforms between CCFv3 (Fig. 5, C and D) and the stereotaxic correction demonstrated (Fig. 5, G and H) were applied to the CCFv3 labels to estimate the changes upon stereotaxic correction. Figure S10 compares nine of the larger volume changes in that transformation, showing that volumes in CCFv3 space are up to 8.5% larger and there is a relatively large variation in the change. The differential swelling along x and y and shrinkage along z mean that comparison of relative volumes in CCFv3 space is problematic. Figure S11 demonstrates that there are both decreases and increases in ROI volume upon transformation to the stereotaxic space and the correction ranges from ~−25 to +15%.

The correction for differential shrinkage in z and swelling in x and y in the CCFv3 places the CCFv3 and FP atlases in close alignment due to the angular correction along z, a distortion that is not as prominent in FP (see figs. S5 and S6). However, now, the agreement between coronal sections in the corrected CCFv3 and FP is very good. Perhaps the correction improves estimates of structural volumes crucial in following quantitative volume change in brain development, age-associated neurodegeneration, and across strains.

A final benefit to the correction of the CCFv3 arises from the additional information from MRH to assist imaging pipelines in delineating mesoscale anatomy, as depicted in figs. S12 and S13. There are several existing pipelines that map the CCFv3 (and labels) to optical images (confocal and LSM) (*9*, *27*–*30*). These work well for the healthy male C57BL/6J mice. The challenge comes with different strains and ages. A catalog of MRH and LSM volumes in the common space with labels provides multiple templates for anatomic delineation where boundaries are less clearly defined. In fig. S12, cortical layers are better defined in the DMBA-MD, DMBA-AD, and DMBA-DWI volumes than the CCFv3. Boundaries of thalamic nuclei are much better circumscribed in the DMBA-MD with complimentary information from the DWI than the same regions in the CCFv3. The fiber orientation displayed in the color FA (fig. S12G) resolves fimbria (yellow) from stria terminalis (blue) and internal capsule (red) in a region devoid of signal in the CCFv3 atlas. In the magnified hippocampus in fig. S13, differential contrast in the DMBA-AD, DMBA-DWI, and DMBA-FA helps delineate and differentiate the cell-dense layers (granular layer of the dentate gyrus and pyramidal cells layers of the CA fields) from the neuropil-rich layers of the hippocampal divisions. Moreover, these DMBA MRH contrasts reveal sublaminar structure in the CA fields, such as the differentiation of the stratum lacunosum moleculare from the stratum radiatum in CA1 (see fig. S13, F and G).

Figure S14 highlights the anatomic insight provided by the TDIs. Calamante *et al.* reported the super-resolution method in 2010 (*10*). They compared super-resolution TDIs in a mouse brain to conventional histological sections stained for myelin using Gallyas silver stain in a mouse brain in 2012 (*31*). Their data were acquired with a Stesjkal Tanner spin echo sequence encoding at 100-μm isotropic resolution with 30 directions at $b = 5000$ s/mm^2. Super-resolution construction allowed them to extend the spatial resolution down to 20 μm. The data in the DMBA were acquired with 15 μm^3 voxels that are ~300 times smaller with 108 angular samples (resolution index that is more than 1000X larger), allowing us to use a step size of 5 μm. The light sheet volume (Specimen 200316-1) stained with myelin basic protein was registered using the NeuN image, which was one channel of the acquisition (table S4). The data in fig. S14 use the method described by Calamante *et al.* to address the dynamic range by constraining the length of the local neighborhood contributing to the display to <1 mm.

Calamante *et al.* (*31*) points out the challenge in the comparisons between TDI and myelin arising from the inherently different mechanisms giving rise to each image. Structures other than myelinated axonal fascicles can readily yield signal in the TDI, as discussed above for the neocortex. Similarly, a comparison of Thy-1 expression in the hippocampus with TDI signal indicates that TDI is capturing anisotropy associated with the organization of neuronal dendrites and axonal projections (fig. S15).

Multiple light sheet volumes mapped to the same stereotaxic space

The stereotaxic atlas allows one to correct for differential processing distortions, supporting comparison of true cell density across multiple specimens (*9*, *32*). Figure S16 and the accompanying video summarize the process by which an arbitrary light sheet volume can be placed into the stereotaxic space using the multiple volumes of the DMBA. To demonstrate this potential, four specimens (Specimens 220905-1, 2, 3, and 4) were processed with immunohistochemical labels summarized in table S4. Note that these specimens were not scanned with MRH. They were mapped to the DMBA space through the NeuN MDT (see Materials and Methods). The precision of alignment is demonstrated in Fig. 6. Because the four volumes have been corrected for geometric distortions from extraction from the skull, tissue clearing, and differential staining, it is possible to make quantitative comparisons of neuron density using the methods outlined in (*32*). The caveat is that the normalization is to an average. Figure S17 shows the corrected neuron density in CA1, CA3, subiculum, and LGD for the all the specimens. The spread in the density derived from the modified stereological fractionator provides insight into the heterogeneity of the neurons in each ROI.

DISCUSSION

Neuroscience spans scales from live animal studies (e.g., electrophysiologists and preclinical MRI at 0.1 mm^3 to the cellular level, e.g., The Brain Initiative Cell Census Network (BICCN) at 1 μm^3 (*33*–*36*). Regional volume estimates are crucial for preclinical MRI and micro–positron emission tomography studies of aging and neurodegeneration. Geneticists need atlases that will translate across strains (*14*). There have been numerous creative approaches to address this cross-disciplinary need (*29*, *30*, *37*–*43*). The DMBA assembles in a single stereotaxic volume the best of all these previous efforts with MRH with spatial resolution at least an order of magnitude higher than any previous work. This spatial resolution approaches the limits set by diffusion (*44*). Our unique high field instrument with extremely powerful gradients allows us to minimize the diffusion encoding time while optimizing the diffusion contrast. This, in turn, yields improved contrast resolution in 14 widely varied sources of anatomic contrast, with diffusion tensor data. The resolution index is more than two orders of magnitude beyond anything published previously. We have added full-resolution light sheet volumes of 17 different molecular and cellular stains and a subset of the CCFv3

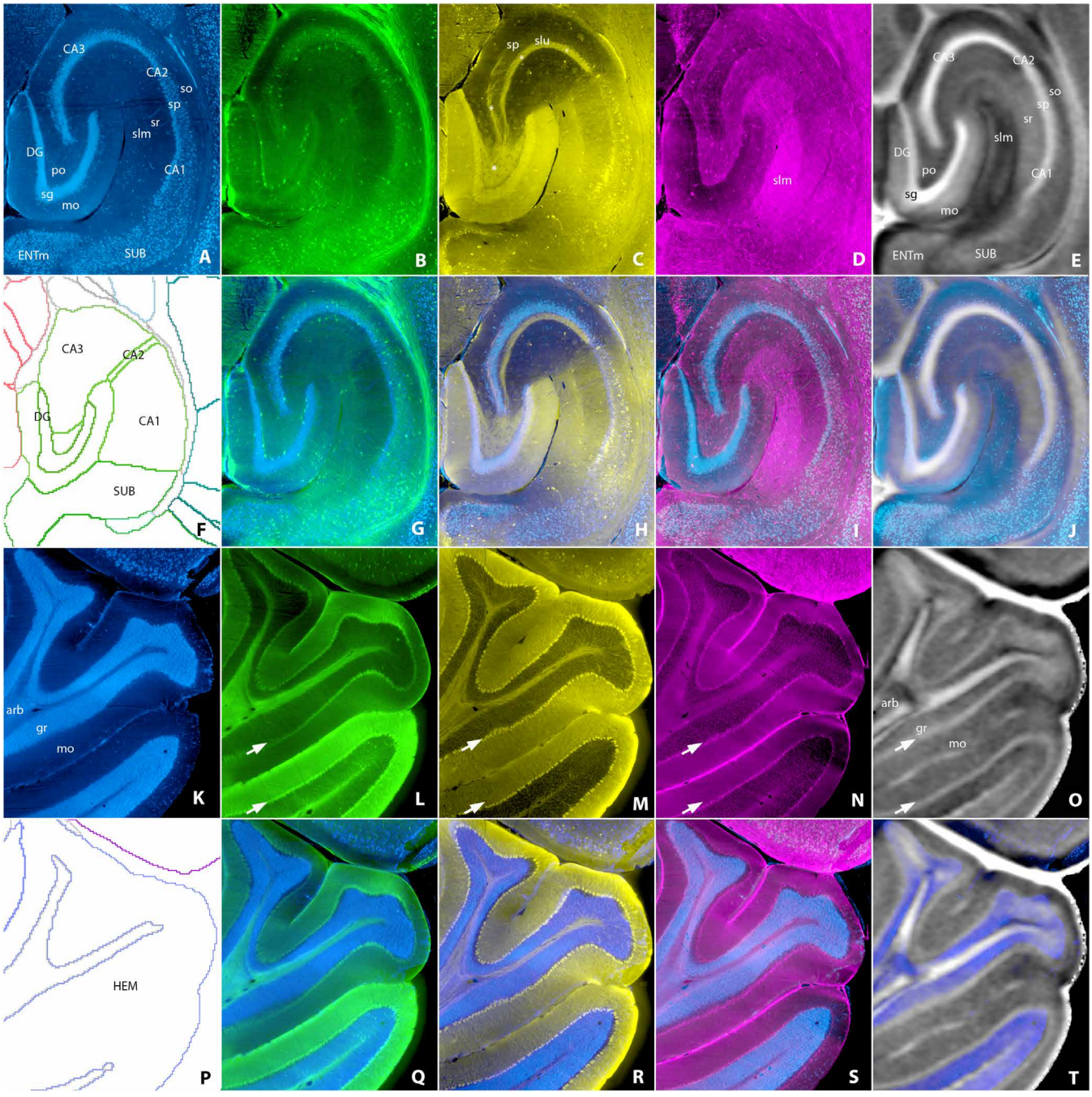

Fig. 6. LSM from four different animals have been coregistered into the DMBA. Rows 1 and 2 show the hippocampus, and rows 3 and 4 show the lateral cerebellar cortex. In each case, the first row shows images from individual specimen after alignment to the DMBA and the second row shows overlays to demonstrate alignment between specimens. (**A** and **K**) NeuN, with AMBA labels; (**B** and **L**) parvalbumin; (**C** and **M**) calbindin; (**D** and **N**) neuropeptide Y; (**E** and **O**) axial diffusivity; and (**F** and **P**) DMBS atlas labels. In the second row of merged panels, note the registration within 20 μm of the cell-dense layers of the hippocampus across volumes (e.g., DG and CA3). In (H), note the precision of the registration where the pyramidal cell layer of CA3 fits within the distribution of mossy fibers of dentate granule cells [marked by asterisks in (C), including the slu, which are immunoreactive for calbindin]. In the cerebellar cortex, note the registration of the granule cell layer and the Purkinje layer (marked with open triangles), including the axial diffusivity image where the Purkinje layer gives rise to a distinct band of moderate signal. Abbreviations: arb, arbor vitae; CA1-3, Ammon's horn fields 1-3; DG, dentate gyrus; ENTm, entorhinal cortex medial part; gr, cerebellum granular layer; HEM, cerebellum hemisphere; mo, cerebellum molecular layer; mo, dentate gyrus molecular layer; po, dentate gyrus polymorph layer; sg, dentate gyrus granule cell layer; slu, stratum lucidum; slm, stratum lacunosum moleculare; so, stratum oriens; sp, pyramidal layer; sr, stratum radiatum; SUBR, subiculum region; SUBv, subiculum ventral part. Different lookup tables were used in Imaris to highlight the different fluorescent markers in each panel. The brightness and contrast in each panel were adjusted independently in Photoshop. Video at https://bit.ly/sa-figure6.

delineations. The breadth and depth of the DMBA can be used to bring other atlases into the same stereotaxic space to integrate differing ontologies and make more accurate and biologically meaningful comparisons.

Expansion of the DMBA is underway. The raw file from which connectomes can be generated has been registered to the ABA retroviral tracer volume (*45*) to generate a white matter atlas. MRH volumes have been acquired on at least 30 different strains of mice at different ages. Additional immunohistochemistry volumes have been acquired and registered to the common space. More than 400 specimens from over 20 different strains of mice have now been mapped into the stereotaxic space with RCCFv3 labels in the DMBA, creating libraries of atlases demonstrating age- and strain-related differences. Training with over 100 specimens has begun to support automated artificial intelligence segmentation. Version v2025-03-04 is available through CIVMImageSpace. As updates become available, they will be made available through the site. We are confident that the DMBA can become a critical tool in integrating mouse brain studies across the scales that span the ever-increasing breadth of contemporary neuroscience.

MATERIALS AND METHODS

Specimen preparation

All animal procedures were approved by the Duke Institutional Animal Care and Use Committee (Duke IACUC approval A169-20-08). Male C57BL/6J mice and adult B6.Cg-Tg (Thy1-YFG/HJrs/J) were purchased from the Jackson Laboratory. All animals were perfused with 10% ProHance (gadoteridol) in buffered formalin. ProHance is a chelated gadolinium compound commonly used in clinical MRI as a contrast agent. It is used as an active stain in MRH to reduce the spin-lattice relaxation time (T1) from 1800 to ~100 ms (*46*, *47*). Animals were anesthetized to a surgical plane with pentobarbital. A 21-gauge needle connected to a peristaltic pump was inserted in the left ventricle. Blood was flushed using a 0.1% heparin saline solution, followed by perfusion with the ProHance/formalin mixture for ~6 min. Heads were placed in buffered formalin for an additional 24 hours. Mandibles were removed, the skin and muscle were removed to allow use of a smaller radiofrequency coil, and brains in the cranium were placed in an 0.5% ProHance/buffer solution and allowed to equilibrate for at least 3 weeks (*48*).

MR acquisition

MRH images were acquired on a 9.4-T/89-mm vertical bore magnet with an Agilent Direct Drive console (Vnmrj 4.0). A Resonance Research (Billerica, MA) Model BRG-88_41 coil provided peak gradients up to 2500 mT/m. The brain was placed in a solenoid coil constructed from a single sheet of silver foil. Two 3D imaging sequences were used: an mGRE ($n = 4$) sequence repetition time (TR = 100 ms) and echo time (TE = 4 ms) and a Stesjkal/Tanner spin echo sequence (*49*) for DTI (TR/TE = 100/12 to 19 ms). Both sequences used phase encoding along the short axes of the specimen (x and y) with the readout gradient applied along the long axis of the specimen (z). Both sequences were accelerated using compressed sensing with an acceleration factor of 8X (*50*). Two different sets of dMRI experiments were performed: one group ($n = 17$) @ 25-μm isotropic resolution and a second group ($n = 5$) @ 15-μm isotropic resolution. All used $b = 3000$ s/mm^2. The 15-μm set was downsampled to 25 μm, and the DWIs from all 22 specimens were used to create the population atlas MDT (see DMBA MDT creation). The 15-μm ($n = 5$) images were registered at full resolution to the MDT to create the MR atlas. Each of these five datasets was acquired with 108 volumes with angular samples of diffusion gradients equally distributed on the unit sphere with $b = 3000$ s/mm^2 with TR = 100 ms and TE = 16 ms with a single excitation for each line of Fourier space. A baseline (b_0) image was acquired after each 10 diffusion encoded volumes (*7*). Data were acquired on an 1134 x 992 x 992 matrix over a field of view of 17.01 by 14.88 by 14.88 mm at 15-μm isotropic resolution.

DMBA MDT creation

The population average ($n = 22$) was generated by creating an MDT of the DWI of all 22 specimens using our SAMBA pipeline (*12*). The pipeline is based on the Advanced Normalization Tool set (ANTs) (*13*). All 22 DWI volumes were first masked to remove the skull. Registration was initialized by a rigid alignment to our existing reference atlas (*7*). An initial MDT template was created using a pairwise affine registration. For each volume, an affine transform was calculated to every other volume in the group. These were averaged together using the ANTs averageAffineTransforms.exe command to create an initial MDT, which is the average of all 22 individuals. This was followed by an iterative diffeomorphic registration process where, in each iteration, all specimens were diffeomorphically registered to the previous template using the cross-correlation metric and symmetric normalization (SyN) registration. The previously computed rigid and pairwise affine transforms were used as initializers. We applied these transforms and averaged the resulting volumes together to create the next template. This was repeated six times. The transforms generated were applied to the five 15-μm volumes to create the MRH volumes for the DMBA. This template was cropped to 750 x 600 x 1260 (the equivalent of 600 axial, 750 sagittal, and 1260 coronal cardinal images). Once we generated the final template, we cropped the volume and rigidly warped it to a stereotactic space, based on skull landmarks derived from the micro-CT scan.

CT acquisition

CT data were acquired on a Nikon XT H 225 ST high-resolution CT scanner in the Duke Shared Material Instrumentation Facility. Specimens were mounted in a 1-inch acrylic centrifuge tube using open cell foam to hold the tissue in place. The tube was filled with normal saline to reduce the potential for projection over ranging. Scans were acquired at 130 kVp (kilovolt peak) and 190 mA with a 0.125-mm Cu filter using 300 projections, resulting in isotropic 25-μm isotropic resolution.

CT registration and stereotaxic orientation

The DMBA stereotaxic space was defined using cranial landmarks extracted from a micro-CT dataset of the mouse skull. Using 3D Slicer, we manually placed ~100 landmarks each along the sagittal suture, coronal suture, and lambdoid suture. A curve of best fit was calculated through each suture. For the sagittal suture, a polynomial curve was fit. Because of their more complex shape, the coronal and lambdoid sutures were fit with the discrete cosine transform. Before finding the curve intersections, we registered the CT scan to the DMBA MRH atlas volume in two stages. First, we created a brain tissue mask of the CT volume with thresholding and manual edits. This mask was affinely registered to a mask of the DMBA-DWI volume. Then, we refined the registration using the Slicer Landmark Registration module with a thin plate spline transform. With the CT

scan aligned with the MR and in RAS orientation, we defined bregma as the intersection of the sagittal and coronal best fit curves, projected to the surface of the skull. RAS describes the orientation of the images from the subject's perspective with *X* pointing toward the right side of the head, *Y* pointing toward the anterior aspect of the head, and *Z* pointing toward the superior aspect of the head. We define lambda as the intersection of the sagittal and lambdoid best fit curves, projected to the surface of the skull. To fully define the stereotaxic space (to find the correct left-right rotation so the axial slices are not skewed), we placed a third landmark at the decussation of the AC, as identified by the RCCF label set that has been registered to the atlas volume. The volume was rotated such that bregma and lambda lay on the same axial slice, and all three landmarks lay on the same sagittal slice. The volume was then translated so that its origin is at bregma. The process was repeated on all five specimens. The average bregma-lambda distance was 4.31 ± 0.31 mm. We choose the largest specimen 230328-4:1 with bregma-lambda of 4.67 mm as the reference for the atlas.

LSM acquisition

Upon completion of MR/DTI acquisition, the brains were removed from the skull, placed in buffered saline, and shipped to LifeCanvas Technology (Cambridge, MA) for light sheet imaging. Formalin-fixed samples were preserved using SHIELD following the outline described in (*51*). Each brain was incubated in 20 ml of SHIELD-off solution for 4 days followed by 1 day of incubation in 20 ml of SHIELD-on solution. The meninges were then removed from each sample. Samples were incubated in Clearing Buffer A (LifeCanvas Technologies) overnight then actively delipidated using a LifeCanvas Technologies SmartClear II Pro device for 6 days using stochastic electrotransport (*52*). After depilation, the samples were washed in phosphate-buffered saline (PBS) with 0.1% Tween 20 for 1 day to remove SDS. For immunolabeling, the samples were incubated in SmartLabel Primary Sample Buffer (LifeCanvas Technologies) overnight with an additional 5- to 6-hour incubation with fresh buffer before primary immunolabeling in a SmartLabel device using eFLASH technology, which integrates stochastic electrotransport (*52*) and SWITCH (*53*) for 14 hours. The samples were then washed in PBS for 7 to 8 hours before overnight fixation in 4% paraformaldehyde followed by incubation in secondary labeling buffer at 37°C with two refreshes over the course of 7 to 8 hours before secondary labeling in the SmartLabel device. Table 1 summarizes the labels used. Specimens were scanned using a structured plane illumination microscope in the axial plane with spatial resolution of 1.8 by 1.8 by 4.0 μm over the field of view of 14.9 by 14.9 by 17 mm. Three separate lasers generated excitation at 488, 561, and 647 nm, producing three registered volumes of 250 to 300 GB per channel. This generates the equivalent of ~3725 axial slices, 9400 coronal slices, and 8300 sagittal slices for each channel.

LSM registration to the DMBA

There are three registration pathways for LSM data, depending on the status of the specimen from which it came.

Table 1. Antibodies used for LSM. The first eight specimens were scanned with MRH followed by removal of the brain from the skull and processing/scanning for LSM. The second group of specimens (No MRH) was perfusion fixed as the first group, but no MRH was performed. After fixation, brains were removed and processed for LSM. This group was created to test the potential for registering LSM to the DMBA in the absence of the MRH.

Specimen ID	Antibody/488 channel	Antibody/561 channel	Antibody/647 channel
Combined MRH/LSM			
190415-2:1	Endogenous YFP		
191209-1:1	24 μl of Thermo Fisher Scientific Syto16	20 μg of EnCor Biotechnology Mouse MBP	3 μg of Cell Signaling Technology Rabbit NeuN
200302-1:1	Autofluorescence	25 μg of EnCor Biotechnology Mouse MBP	3 μg of Cell Signaling Technology Rabbit NeuN
200316-1:1	Autofluorescence	25 μg of EnCor Biotechnology Mouse MBP	3 μg of Cell Signaling Technology Rabbit NeuN
200826-1:1	6 μg of Cell Signaling Technology Rabbit NeuN	6 μg of Santa Cruz Biotechnology Rat Somatostatin	40 μl of MilliporeSigma Goat ChAT
201026-1:1	6 μg of Cell Signaling Technology Rabbit NeuN	10 μg of Abcam Goat Parvalbumin	20 μg of EnCor Biotechnology Mouse NF-H
210823-6:2	6 μg of Cell Signaling Technology Rabbit NeuN	80 μl of Vector Labs Lectin DyLight 594	6 μg of BioLegend Mouse Tyrosine Hydroxylase (TH)
210823-8:2	Autofluorescence	10 μg of Thermo Fisher Scientific Mouse GAD67	6 μg of Abcam Rabbit Dopamine Beta Hydroxylase (DBH)
No MRH			
220905-1	10 μg of R&D Systems Goat CD31	10 μg of EnCor Biotechnology Mouse NeuN	10 μg of Thermo Fisher Scientific Rabbit Parvalbumin
220905-2	10 μg of R&D Systems Goat CD31	10 μg of EnCor Biotechnology Mouse NeuN	10 μg of Cell Signaling Technology Rabbit Calbindin
220905-3	10 μg of R&D Systems Goat CD31	10 μg of EnCor Biotechnology Mouse NeuN	6 μg of Abcam Rabbit VIP
220905-4	10 μg of R&D Systems Goat CD31	10 μg of EnCor Biotechnology Mouse NeuN	6 μg of Cell Signaling Technology Rabbit Neuropeptide Y

Light sheet volumes of specimens in the combined MRH/LSM template group (table S2) were aligned to the MRH volume of the same specimen using methods outlined in detail in (*9*). This is a three-step registration process, starting with a coarse manual landmark registration in Slicer to account for the major tissue tearing, nonlinear swelling, and distortions. There are generally distortions throughout the brain, but they are most extreme in the olfactory bulb and brainstem. DWI was the target volume contrast, and NeuN was used as the moving volume contrast. Registration was performed at 15-μm resolution. The next step was a two-stage diffeomorphic registration using the antsRegistration from ANTs (*13*). Stage one used the BSplineSyN transform and cross-correlation metric. This result was pushed to a refinement stage using the SyN transform and Mattes metric. These transforms and those computed to create the DMBA template were then applied to the full-resolution LSFM volume to warp into the DMBA stereotaxic space. The quality of the registration was evaluated for multiple combinations of MRH contrast and fluorescent label using the L2 norm with three different datasets with fiducial landmarks ($n = 50$, $n = 175$, and $n = 200$) on the MRH and LSM. Results of this systematic comparison are summarized in Table S2 in ref. (*9*). The combination of NeuN with DWI yielded the best results with a global L2 norm of 135 μm. The limitation in this approach was the precision with which landmarks could be assigned to both MRH and LSM. A second approach used branching vessels, which provided a more reproducible method of labeling both MRH and LSM volumes. Using this method resulted in a mean error of alignment of 22 μm across the 3D volume (fig. S3) (*9*).

A second group of four LSM datasets (table S2, specimens 220905-1:1 to 4:1) was acquired on specimens for which there were no MRH scans. The previous approach would not work because the first stage correction to an MRH volume was not possible. We instead created a group template using SAMBA as was used to create the DMBA MRI template. LSM NeuN volumes were downsampled to 45 μm. We performed N4 bias correction (*54*) to remove staining bias, and applied a log scale to accommodate the dynamic range. Because we do not have an existing LSM atlas volume, one individual was arbitrarily chosen as the target for the rigid transform initialization stage. After all transforms were calculated, they were applied to the LSM volumes at 15 μm without the bias correction or log scaling. This LSM template was then registered to the MRH atlas using the pipeline described above, with this NeuN template as the moving volume and the DMBA-DWI template as the registration target. Because both are average volumes, some individual variability is smoothed out and registration is more successful. This approach also only requires one manual landmark registration job instead of N, reducing the amount of human error in the results.

Last, this NeuN template registered to the DMBA provided a gateway to register arbitrary LSM volumes into the common space. Volumes were downsampled to 45 μm, bias corrected, and log scaled. A rigid and affine initialization to the NeuN template were performed, followed by a diffeomorphic registration using the cross-correlation metric and SyN registration. This transform stack (rigid initialization, affine initialization, and diffeomorphic registration to NeuN template) plus all transforms from the NeuN template to the DMBA-DWI template were applied to the full-resolution version of the input volume to warp it into the DMBA stereotaxic space. Although this approach does not have the same accuracy as the other two presented, it is an effective solution to warp arbitrary native-space light sheet volumes (that include NeuN or autofluorescence as a channel) into the DMBA stereotaxic space.

Image processing

Image processing was facilitated by the BigImage environment described in (*7*). 3D slicer (https://slicer.org/) and Imaris 10.0 and 10.1 (https://imaris.oxinst.com/) were used in preparing the figures. A dedicated server receives LSM data via Globus and converts the three channels in each specimen (~300 GB per channel) to tiff stacks. Raw (32 bit) images from the MRH pipelines described above and tiff stacks from the Nikon MicroCT and LifeCanvas were converted to ims format using the file converter (ImarisFileConverter 10.0) provided by Oxford Instruments. When image comparisons were made (e.g., Figs. 1, 2, 3, and 6), all the volumes in a figure were loaded into Imaris at once. This was accomplished on one of our (*4*) high-performance Dell servers, each of which has 2 TB of memory. Imaris is designed for 4D imaging with independent interactive adjustment of lookup tables for each volume. The metadata on each volume of the DMBA have been adjusted to place the original at bregma as described above. Imaris accommodates the varied spatial resolutions (LSM@ 1.8 by 1.8 by 4.0 μm, TDI @ 5 μm, MRH @ 15 μm, and micro-CT @ 25 μm) by scaling the data internally. Imaris provides a fiducial bar that was captured in each image being compared and carried through in assembling figures to provide provenance on spatial resolution. When assembling figures with multiple resolutions, care was taken to load the highest-resolution data first, which assures that slices being compared are done so at their native slice thickness unless purposely overridden. Minimum, maximum, and gamma are adjusted to map the histogram of the volume to the available gray (or color) scale. Individual frames are captured at the Nyquist resolution of the image being shared. Final figure assembly takes place in Photoshop and Illustrator where gray or color scale from the individual components of the images (from different modalities) are fine-tuned by adjusting the minimum, maximum, and gamma to the available range in the figure. In some cases, scale bars in the final composite are then edited out.

Supplementary Materials

The PDF file includes:

Figs. S1 to S17
Tables S1 to S5
Legends for movies S1 to S3
References

Other Supplementary Material for this manuscript includes the following:

Movies S1 to S3

REFERENCES AND NOTES

1. K. B. J. Franklin, G. Paxinos, *The Mouse Brain in Stereotaxic Coordinates* (Academic Press, 1997).
2. K. B. J. Franklin, G. Paxinos, *The Mouse Brain in Sterotaxic Coordinates, Fifth Edition* (Elsevier Science, 2019).
3. H. W. Dong, *The Allen Reference Atlas: A Digital Color Brain Atlas of the C57Bl/6J Male Mouse* (Wiley, 2008).
4. Q. Wang, S. L. Ding, Y. Li, J. Royall, D. Feng, P. Lesnar, N. Graddis, M. Naeemi, B. Facer, A. Ho, T. Dolbeare, B. Blanchard, N. Dee, W. Wakeman, K. E. Hirokawa, A. Szafer, S. M. Sunkin, S. W. Oh, A. Bernard, J. W. Phillips, M. Hawrylycz, C. Koch, H. Zeng, J. A. Harris, L. Ng, The Allen Mouse Brain Common Coordinate Framework: A 3D reference atlas. *Cell* **181**, 936–953.e20 (2020).
5. G. A. Johnson, A. Badea, J. Brandenburg, G. Cofer, B. Fubara, S. Liu, J. Nissanov, Waxholm space: An image-based reference for coordinating mouse brain research. *Neuroimage* **53**, 365–372 (2010).
6. G. A. Johnson, H. Benveniste, R. D. Black, L. W. Hedlund, R. R. Maronpot, B. R. Smith, Histology by magnetic resonance microscopy. *Magn. Reson. Q.* **9**, 1–30 (1993).

7. G. A. Johnson, Y. Tian, D. G. Ashbrook, G. P. Cofer, J. J. Cook, J. C. Gee, A. Hall, K. Hornburg, C. C. Kaczorowski, Y. Qi, F. C. Yeh, N. Wang, L. E. White, R. W. Williams, Merged magnetic resonance and light sheet microscopy of the whole mouse brain. *Proc. Natl. Acad. Sci. U.S.A.* **120**, e2218617120 (2023).
8. G. Feng, R. H. Mellor, M. Bernstein, C. Keller-Peck, Q. T. Nguyen, M. Wallace, J. M. Nerbonne, J. W. Lichtman, J. R. Sanes, Imaging neuronal subsets in transgenic mice expressing multiple spectral variants of GFP. *Neuron* **28**, 41–51 (2000).
9. Y. Tian, J. J. Cook, G. A. Johnson, Restoring morphology of light sheet microscopy data based on magnetic resonance histology. *Front. Neurosci.* **16**, 1011895 (2022).
10. F. Calamante, J.-D. Tournier, G. D. Jackson, A. Connelly, Track-density imaging (TDI): Super-resolution white matter imaging using whole-brain track-density mapping. *Neuroimage* **53**, 1233–1243 (2010).
11. K. B. J. Franklin, G. Paxinos, *The Mouse Brain in Stereotaxic Coordinates, Third Edition* (Elsevier Science, 2008).
12. R. J. Anderson, J. J. Cook, N. Delpratt, J. C. Nouls, B. Gu, J. McNamara, B. B. Avants, G. A. Johnson, A. Badea, Small animal multivariate brain analysis (SAMBA)—A high throughput pipeline with a validation framework. *Neuroinformatics* **17**, 451–472 (2019).
13. B. B. Avants, N. J. Tustison, M. Stauffer, G. Song, B. Wu, J. C. Gee, The Insight ToolKit image registration framework. *Front. Neuroinform.* **8**, 44 (2014).
14. N. Wang, R. J. Anderson, D. G. Ashbrook, V. Gopalakrishnan, Y. Park, C. E. Priebe, Y. Qi, R. Laoprasert, J. T. Vogelstein, R. W. Williams, G. A. Johnson, Variability and heritability of mouse brain structure: Microscopic MRI atlases and connectomes for diverse strains. *Neuroimage* **222**, 117274 (2020).
15. F.-C. Yeh, V. J. Wedeen, W. Y. I. Tseng, Generalized q-sampling imaging. *IEEE Trans. Med. Imaging* **29**, 1626–1635 (2010).
16. F. C. Yeh, W. Y. Tseng, NTU-90: A high angular resolution brain atlas constructed by q-space diffeomorphic reconstruction. *Neuroimage* **58**, 91–99 (2011).
17. P. J. Basser, D. K. Jones, Diffusion-tensor MRI: Theory, experimental design and data analysis—A technical review. *NMR Biomed.* **15**, 456–467 (2002).
18. S. Mori, B. J. Crain, V. P. Chacko, P. C. van Zijl, Three-dimensional tracking of axonal projections in the brain by magnetic resonance imaging. *Ann. Neurol.* **45**, 265–269 (1999).
19. A. W. Toga, K. A. Clark, P. M. Thompson, D. W. Shattuck, J. D. Van Horn, Mapping the human connectome. *Neurosurgery* **71**, 1–5 (2012).
20. E. Calabrese, A. Badea, G. Cofer, Y. Qi, G. A. Johnson, A diffusion MRI tractography connectome of the mouse brain and comparison with neuronal tracer data. *Cereb. Cortex* **25**, 4628–4637 (2015).
21. D. S. Tuch, T. G. Reese, M. R. Wiegell, N. Makris, J. W. Belliveau, V. J. Wedeen, High angular resolution diffusion imaging reveals intravoxel white matter fiber heterogeneity. *Magn. Reson. Med.* **48**, 577–582 (2002).
22. D. K. Jones, T. R. Knösche, R. Turner, White matter integrity, fiber count, and other fallacies: The do's and don'ts of diffusion MRI. *Neuroimage* **73**, 239–254 (2013).
23. K. Ugurbil, J. Xu, E. J. Auerbach, S. Moeller, A. T. Vu, J. M. Duarte-Carvajalino, C. Lenglet, X. Wu, S. Schmitter, P. F. Van de Moortele, J. Strupp, G. Sapiro, F. De Martino, D. Wang, N. Harel, M. Garwood, L. Chen, D. A. Feinberg, S. M. Smith, K. L. Miller, S. N. Sotiropoulos, S. Jbabdi, J. L. R. Andersson, T. E. J. Behrens, M. F. Glasser, D. C. Van Essen, E. Yacoub, WU-Minn HCP Consortium, Pushing spatial and temporal resolution for functional and diffusion MRI in the Human Connectome Project. *Neuroimage* **80**, 80–104 (2013).
24. B. Wilkins, N. Lee, N. Gajawelli, M. Law, N. Leporé, Fiber estimation and tractography in diffusion MRI: Development of simulated brain images and comparison of multi-fiber analysis methods at clinical b-values. *Neuroimage* **109**, 341–356 (2015).
25. K. H. Maier-Hein, P. F. Neher, J.-C. Houde, M.-A. Côté, E. Garyfallidis, J. Zhong, M. Chamberland, F.-C. Yeh, Y.-C. Lin, Q. Ji, W. E. Reddick, J. O. Glass, D. Q. Chen, Y. Feng, C. Gao, Y. Wu, J. Ma, R. He, Q. Li, C.-F. Westin, S. Deslauriers-Gauthier, J. O. O. González, M. Paquette, S. St-Jean, G. Girard, F. Rheault, J. Sidhu, C. M. W. Tax, F. Guo, H. Y. Mesri, S. Dávid, M. Froeling, A. M. Heemskerk, A. Leemans, A. Boré, B. Pinsard, C. Bedetti, M. Desrosiers, S. Brambati, J. Doyon, A. Sarica, R. Vasta, A. Cerasa, A. Quattrone, J. Yeatman, A. R. Khan, W. Hodges, S. Alexander, D. Romascano, M. Barakovic, A. Auría, O. Esteban, A. Lemkaddem, J.-P. Thiran, H. E. Cetingul, B. L. Odry, B. Mailhe, M. S. Nadar, F. Pizzagalli, G. Prasad, J. E. Villalon-Reina, J. Galvis, P. M. Thompson, F. D. S. Requejo, P. L. Laguna, L. M. Lacerda, R. Barrett, F. Dell'Acqua, M. Catani, L. Petit, E. Caruyer, A. Daducci, T. B. Dyrby, T. Holland-Letz, C. C. Hilgetag, B. Stieltjes, M. Descoteaux, The challenge of mapping the human connectome based on diffusion tractography. *Nat. Commun.* **8**, 1349 (2017).
26. G. A. Johnson, N. Wang, R. J. Anderson, M. Chen, G. P. Cofer, J. C. Gee, F. Pratson, N. Tustison, L. E. White, Whole mouse brain connectomics. *J. Comp. Neurol.* **527**, 2146–2157 (2019).
27. N. Renier, E. L. Adams, C. Kirst, Z. Wu, R. Azevedo, J. Kohl, A. E. Autry, L. Kadiri, K. U. Venkataraju, Y. Zhou, V. X. Wang, C. Y. Tang, O. Olsen, C. Dulac, P. Osten, M. Tessier-Lavigne, Mapping of brain activity by automated volume analysis of immediate early genes. *Cell* **165**, 1789–1802 (2016).
28. M. Goubran, C. Leuze, B. Hsueh, M. Aswendt, L. Ye, Q. Tian, M. Y. Cheng, A. Crow, G. K. Steinberg, J. A. McNab, K. Deisseroth, M. Zeineh, Multimodal image registration and connectivity analysis for integration of connectomic data from microscopy to MRI. *Nat. Commun.* **10**, 5504 (2019).
29. J. Perens, C. G. Salinas, J. L. Skytte, U. Roostalu, A. B. Dahl, T. B. Dyrby, F. Wichern, P. Barkholt, N. Vrang, J. Jelsing, J. Hecksher-Sørensen, An optimized mouse brain atlas for automated mapping and quantification of neuronal activity using iDISCO+ and light sheet fluorescence microscopy. *Neuroinformatics* **19**, 433–446 (2021).
30. J. Perens, C. G. Salinas, U. Roostalu, J. L. Skytte, C. Gundlach, J. Hecksher-Sørensen, A. B. Dahl, T. B. Dyrby, Multimodal 3D mouse brain atlas framework with the skull-derived coordinate system. *Neuroinformatics* **21**, 269–286 (2023).
31. F. Calamante, J. D. Tournier, N. D. Kurniawan, Z. Yang, E. Gyengesi, G. J. Galloway, D. C. Reutens, A. Connelly, Super-resolution track-density imaging studies of mouse brain: Comparison to histology. *Neuroimage* **59**, 286–296 (2012).
32. Y. Tian, G. A. Johnson, R. W. Williams, L. White, A rapid workflow for neuron counting in combined light sheet microscopy and magnetic resonance histology. *Front. Neurosci.* **17**, 1223226 (2023).
33. N. R. Zemke, E. J. Armand, W. Wang, S. Lee, J. Zhou, Y. E. Li, H. Liu, W. Tian, J. R. Nery, R. G. Castanon, A. Bartlett, J. K. Osteen, D. Li, X. Zhuo, V. Xu, L. Chang, K. Dong, H. S. Indralingam, J. A. Rink, Y. Xie, M. Miller, F. M. Krienen, Q. Zhang, N. Taskin, J. Ting, G. Feng, S. A. McCarroll, E. M. Callaway, T. Wang, E. S. Lein, M. M. Behrens, J. R. Ecker, B. Ren, Conserved and divergent gene regulatory programs of the mammalian neocortex. *Nature* **624**, 390–402 (2023).
34. M. Zhang, X. Pan, W. Jung, A. R. Halpern, S. W. Eichhorn, Z. Lei, L. Cohen, K. A. Smith, B. Tasic, Z. Yao, H. Zeng, X. Zhuang, Molecularly defined and spatially resolved cell atlas of the whole mouse brain. *Nature* **624**, 343–354 (2023).
35. J. Zhou, Z. Zhang, M. Wu, H. Liu, Y. Pang, A. Bartlett, Z. Peng, W. Ding, A. Rivkin, W. N. Lagos, E. Williams, C.-T. Lee, P. A. Miyazaki, A. Aldridge, Q. Zeng, J. L. A. Salinda, N. Claffey, M. Liem, C. Fitzpatrick, L. Boggeman, Z. Yao, K. A. Smith, B. Tasic, J. Altshul, M. A. Kenworthy, C. Valadon, J. R. Nery, R. G. Castanon, N. S. Patne, M. Vu, M. Rashid, M. Jacobs, T. Ito, J. Osteen, N. Emerson, J. Lee, S. Cho, J. Rink, H.-H. Huang, A. Pinto-Duartec, B. Dominguez, J. B. Smith, C. O'Connor, H. Zeng, S. Chen, K.-F. Lee, E. A. Mukamel, X. Jin, M. M. Behrens, J. R. Ecker, E. M. Callaway, Brain-wide correspondence of neuronal epigenomics and distant projections. *Nature* **624**, 355–365 (2023).
36. S. Zu, Y. E. Li, K. Wang, E. J. Armand, S. Mamde, M. L. Amaral, Y. Wang, A. Chu, Y. Xie, M. Miller, J. Xu, Z. Wang, K. Zhang, B. Jia, X. Hou, L. Lin, Q. Yang, S. Lee, B. Li, S. Kuan, H. Liu, J. Zhou, A. Pinto-Duarte, J. Lucero, J. Osteen, M. Nunn, K. A. Smith, B. Tasic, Z. Yao, H. Zeng, Z. Wang, J. Shang, M. M. Behrens, J. R. Ecker, A. Wang, S. Preissl, B. Ren, Single-cell analysis of chromatin accessibility in the adult mouse brain. *Nature* **624**, 378–389 (2023).
37. A. MacKenzie-Graham, E. F. Lee, I. D. Dinov, M. Bota, D. W. Shattuck, S. Ruffins, H. Yuan, F. Konstantinidis, A. Pitiot, Y. Ding, G. Hu, R. E. Jacobs, A. W. Toga, A multimodal, multidimensional atlas of the C57BL/6J mouse brain. *J. Anat.* **204**, 93–102 (2004).
38. E. Chan, N. Kovacevíc, S. K. Ho, R. M. Henkelman, J. T. Henderson, Development of a high resolution three-dimensional surgical atlas of the murine head for strains 129S1/SvImJ and C57Bl/6J using magnetic resonance imaging and micro-computed tomography. *Neuroscience* **144**, 604–615 (2007).
39. M. Aggarwal, J. Zhang, M. I. Miller, R. L. Sidman, S. Mori, Magnetic resonance imaging and micro-computed tomography combined atlas of developing and adult mouse brains for stereotaxic surgery. *Neuroscience* **162**, 1339–1350 (2009).
40. C. B. G. Salinas, T. T.-H. Lu, S. Gabery, K. Marstal, T. Alanentalo, A. J. Mercer, A. Cornea, K. Conradsen, J. Hecksher-Sørensen, A. B. Dahl, L. B. Knudsen, A. Secher, Integrated brain atlas for unbiased mapping of nervous system effects following liraglutide treatment. *Sci. Rep.* **8**, 10310 (2018).
41. U. Chon, D. J. Vanselow, K. C. Cheng, Y. Kim, Enhanced and unified anatomical labeling for a common mouse brain atlas. *Nat. Commun.* **10**, 5067 (2019).
42. F. F. Stæger, K. N. Mortensen, M. S. N. Nielsen, B. Sigurdsson, L. K. Kaufmann, H. Hirase, M. Nedergaard, A three-dimensional, population-based average of the C57BL/6 mouse brain from DAPI-stained coronal slices. *Sci. Data* **7**, 235 (2020).
43. L. Qu, Y. Li, P. Xie, L. Liu, Y. Wang, J. Wu, Y. Liu, T. Wang, L. Li, K. Guo, W. Wan, L. Ouyang, F. Xiong, A. C. Kolstad, Z. Wu, F. Xu, Y. Zheng, H. Gong, Q. Luo, G. Bi, H. Dong, M. Hawrylycz, H. Zeng, H. Peng, Cross-modal coherent registration of whole mouse brains. *Nat. Methods* **19**, 111–118 (2022).
44. P. T. Callaghan, *Principles of Nuclear Magnetic Resonance Microscopy* (Oxford Univ. Press, 1991).
45. S. Oh, J. A. Harris, L. Ng, B. Winslow, N. Cain, S. Mihalas, Q. Wang, C. Lau, L. Kuan, A. M. Henry, M. T. Mortrud, B. Ouellette, T. N. Nguyen, S. A. Sorensen, C. R. Slaughterbeck, W. Wakeman, Y. Li, D. Feng, A. Ho, E. Nicholas, K. E. Hirokawa, P. Bohn, K. M. Joines, H. Peng, M. J. Hawrylycz, J. W. Phillips, J. G. Hohmann, P. Wohnoutka, C. R. Gerfen, C. Koch, A. Bernard, C. Dang, A. R. Jones, H. Zeng, A mesoscale connectome of the mouse brain. *Nature* **508**, 207–214 (2014).
46. G. A. Johnson, G. P. Cofer, S. L. Gewalt, L. W. Hedlund, Morphologic phenotyping with MR microscopy: The visible mouse. *Radiology* **222**, 789–793 (2002).
47. G. A. Johnson, L. W. Hedlund, *Three-Dimensional Morphology by Magnetic Resonance Imaging*, U. P. Office, Ed. (Duke University, 2000), vol. 6023162.

48. J. Xiao, K. J. Hornburg, G. Cofer, J. J. Cook, F. Pratson, Y. Qi, G. A. Johnson, A time-course study of actively stained mouse brains: Diffusion tensor imaging parameters and connectomic stability over 1 year. *NMR Biomed.* **35**, e4611 (2022).
49. E. O. Stejskal, J. E. Tanner, Spin diffusion measurements: Spin echoes in the presence of a time-dependent field gradient. *J. Chem. Phys.* **42**, 288–292 (1965).
50. N. Wang, R. J. Anderson, A. Badea, G. Cofer, R. Dibb, Y. Qi, G. A. Johnson, Whole mouse brain structural connectomics using magnetic resonance histology. *Brain Struct. Funct.* **223**, 4323–4335 (2018).
51. Y.-G. Park, C. H. Sohn, R. Chen, M. M. Cue, D. H. Yun, G. T. Drummond, T. Ku, N. B. Evans, H. C. Oak, W. Trieu, H. Choi, X. Jin, V. Lilascharoen, J. Wang, M. C. Truttmann, H. W. Qi, H. L. Ploegh, T. R. Golub, S.-C. Chen, M. P. Frosch, H. J. Kulik, B. K. Lim, K. Chung, Protection of tissue physicochemical properties using polyfunctional crosslinkers. *Nat. Biotechnol.* **37**, 73–83 (2018).
52. S. Y. Kim, J. H. Cho, E. Murray, N. Bakh, H. Choi, K. Ohn, L. Ruelas, A. Hubbert, M. McCue, S. L. Vassallo, P. J. Keller, K. Chung, Stochastic electrotransport selectively enhances the transport of highly electromobile molecules. *Proc. Natl. Acad. Sci. U.S.A.* **112**, E6274–E6283 (2015).
53. E. Murray, J. H. Cho, D. Goodwin, T. Ku, J. Swaney, S. Y. Kim, H. Choi, Y. G. Park, J. Y. Park, A. Hubbert, M. McCue, S. Vassallo, N. Bakh, M. P. Frosch, V. J. Wedeen, H. S. Seung, K. Chung, Simple, scalable proteomic imaging for high-dimensional profiling of intact systems. *Cell* **163**, 1500–1514 (2015).
54. N. J. Tustison, B. B. Avants, P. A. Cook, Y. Zheng, A. Egan, P. A. Yushkevich, J. C. Gee, A. Expand, N4ITK: Improved N3 bias correction. *IEEE Trans. Med. Imaging* **29**, 1310–1320 (2010).
55. H. Benveniste, K. Kim, L. Zhang, G. A. Johnson, Magnetic resonance microscopy of the C57BL mouse brain. *Neuroimage* **11**, 601–611 (2000).
56. N. Kovacević, J. T. Henderson, E. Chan, N. Lifshitz, J. Bishop, A. C. Evans, R. M. Henkelman, X. J. Chen, A three-dimensional MRI atlas of the mouse brain with estimates of the average and variability. *Cereb. Cortex* **15**, 639–645 (2005).
57. Y. Ma, P. R. Hof, S. C. Grant, S. J. Blackband, R. Bennett, L. Slatest, M. D. McGuigan, H. Benveniste, A three-dimensional digital atlas database of the adult C57BL/6J mouse brain by magnetic resonance microscopy. *Neuroscience* **135**, 1203–1215 (2005).
58. G. A. Johnson, A. Ali-Sharief, A. Badea, J. Brandenburg, G. Cofer, B. Fubara, S. Gewalt, L. W. Hedlund, L. Upchurch, High-throughput morphologic phenotyping of the mouse brain with magnetic resonance histology. *Neuroimage* **37**, 82–89 (2007).
59. A. E. Dorr, J. P. Lerch, S. Spring, N. Kabani, R. M. Henkelman, High resolution three-dimensional brain atlas using an average magnetic resonance image of 40 adult C57Bl/6J mice. *Neuroimage* **42**, 60–69 (2008).
60. A. A. Sharief, A. Badea, A. M. Dale, G. A. Johnson, Automated segmentation of the actively stained mouse brain using multi-spectral MR microscopy. *Neuroimage* **39**, 136–145 (2008).
61. Y. Jiang, G. A. Johnson, Microscopic diffusion tensor atlas of the mouse brain. *Neuroimage* **56**, 1235–1243 (2011).
62. A. L. Janke, J. F. P. Ullmann, N. D. Kurniawan, G. Paxinos, M. Keller, Z. Yang, K. Richards, G. Egan, S. Petrou, G. Galloway, D. Reutens, 15 μm average mouse models in Waxholm space from 16.4T 30μm images, in *20th Annual ISMRM Scientific Meeting and Exhibition* (International Society of Magnetic Resonance in Medicine, 2012).
63. J. F. Ullmann, C. Watson, A. L. Janke, N. D. Kurniawan, G. Paxinos, D. C. Reutens, An MRI atlas of the mouse basal ganglia. *Brain Struct. Funct.* **219**, 1343–1353 (2014).
64. B. Nie, D. Wu, S. Liang, H. Liu, X. Sun, P. Li, Q. Huang, T. Zhang, T. Feng, S. Ye, Z. Zhang, B. Shan, A stereotaxic MRI template set of mouse brain with fine sub-anatomical delineations: Application to MEMRI studies of 5XFAD mice. *Magn. Reson. Imaging* **57**, 83–94 (2019).
65. D. A. Barrière, A. Ella, F. Szeremeta, H. Adriaensen, W. Même, E. Chaillou, M. Migaud, S. Même, F. Lévy, M. Keller, Brain orchestration of pregnancy and maternal behavior in mice: A longitudinal morphometric study. *Neuroimage* **230**, 117776 (2021).
66. A. Ianuş, J. Carvalho, F. F. Fernandes, R. Cruz, C. Chavarrias, M. Palombo, N. Shemesh, Soma and Neurite Density MRI (SANDI) of the in-vivo mouse brain and comparison with the Allen Brain Atlas. *Neuroimage* **254**, 119135 (2022).
67. N. Rahman, K. Xu, M. D. Budde, A. Brown, C. A. Baron, A longitudinal microstructural MRI dataset in healthy C57Bl/6 mice at 9.4 Tesla. *Sci. Data* **10**, 94 (2023).
68. T. M. Arefin, C. H. Lee, Z. Liang, H. Rallapalli, Y. Z. Wadghiri, D. H. Turnbull, J. Zhang, Towards reliable reconstruction of the mouse brain corticothalamic connectivity using diffusion MRI. *Neuroimage* **273**, 120111 (2023).

Acknowledgments: We are grateful to J. Gladman in the Duke Shared Material Instrumentation Facility for crucial assistance in obtaining the micro-CT data. We are grateful to T. Johnson for editorial and formatting assistance. **Funding:** This work was supported by the National Institute of Neurological Disorders and Stroke grant R01NS120954-01A1 (F.-C.Y. and G.A.J.) and the National Institute on Aging grant R01AG070913-01 (R.W.W. and G.A.J.). **Author contributions:** Conceptualization: R.W.W., L.E.W., and G.A.J. Data curation: H.M., R.A., J.C.C., K.J.H., Y.Q., and Y.T. Formal analysis: H.M., J.C.C., R.W.W., L.E.W., and G.A.J. Methodology: H.M., J.C.C., and F.-C.Y. Resources: F.-C.Y. Software: J.C.C. and F-CY. Supervision: G.A.J. Validation: R.W.W., L.E.W., and G.A.J. Visualization: H.M., F.-C.Y., and G.A.J. Writing—original draft: R.W.W., L.E.W., and G.A.J. Writing—review and editing: R.W.W., L.E.W., and G.A.J. **Competing interests:** The authors declare that they have no competing interests. **Data and materials availability:** The data reported here are available at CIVMImageSpace (https://civmimagespace.civm.duhs.duke.edu/; 2024 Duke University. All Rights Reserved). The data were produced at the Duke School of Medicine, Department of Radiology and Pratt School of Engineering, Department of Biomedical Engineering and are being made available under a Creative Commons CC BY-NC-SA 4.0 License. See this URL for additional information (https://creativecommons.org/licenses/by-nc/4). All other data needed to evaluate the conclusions in the paper are present in the paper and/or the Supplementary Materials.

Submitted 31 May 2024
Accepted 26 March 2025
Published 30 April 2025
10.1126/sciadv.adq8089